

# CFD Analysis of Primary Air Flow Field of a Swirl Injector Using Embedded LES-Based Hybrid Model



Rampada Rana, N. Muthuveerappan, and Saptarshi Basu

**Abstract** Injector plays a pivotal role in meeting requirements of combustion performance in terms of combustion efficiency, flame stability, ignition, lower emissions, etc. In a multi-swirler injector configuration, air flow field inside injector is mainly dictated by primary swirler. Present CFD studies have been attempted to characterize flow field of a conical nozzle fitted with a radial swirler. Embedded LES-based hybrid model has been used where computational domain is divided into three zones which are seamlessly connected by capturing the interface fluid dynamics. In LES zone, both time and spatial scales have been resolved based on the results of a precursor RANS analysis. Analysis is carried out with CFL no. around 2, time step of 1  $\mu$ s. The analysis is reasonably able to capture various unsteadiness (PVC, CTRZ, frequencies, TKE useful for the atomization of liquid fuel) which are not possible to be captured using URANS models.

## *Nomenclature*

<i>CFD</i>	Computational Fluid Dynamics
<i>CFL</i>	Courant-Friedrichs-Lewy
<i>CTRZ</i>	Central Toroidal Recirculation Zone
<i>ELES</i>	Embedded LES
<i>FFT</i>	Fast Fourier Transform
<i>KH</i>	Kelvin-Helmoltz
<i>LDI</i>	Lean Direct Injection
<i>LPP</i>	Lean Premix Prevaporization
<i>LES</i>	Large Eddy Simulation
<i>MPI</i>	Message Passing Interface

---

R. Rana (✉) · N. Muthuveerappan  
Gas Turbine Research Establishment, Bengaluru, Karnataka, India  
e-mail: [rana-rampada.gtre@gov.in](mailto:rana-rampada.gtre@gov.in)

S. Basu  
Department of Mechanical Engineering, Indian Institute of Science, Bengaluru, Karnataka, India

© The Author(s), under exclusive license to Springer Nature Singapore Pte Ltd. 2023  
G. Sivaramakrishna et al. (eds.), *Proceedings of the National Aerospace Propulsion Conference*, Lecture Notes in Mechanical Engineering,  
[https://doi.org/10.1007/978-981-19-2378-4\\_37](https://doi.org/10.1007/978-981-19-2378-4_37)

629

<i>PIV</i>	Particle Image Velocimetry
<i>POD</i>	Proper Orthogonal Decomposition
<i>PVC</i>	Precessing Vortex Core
<i>RANS</i>	Reynolds Averaged Navier Stokes
<i>Re</i>	Reynolds Number
<i>RQL</i>	Rich burn Quick quench Lean burn
<i>SIMPLEC</i>	Semi-Implicit Pressure Linked-Consistent
<i>SGS</i>	SubGrid Scale
<i>TKE</i>	Turbulent Kinetic Energy
<i>URANS</i>	Unsteady RANS
<i>WMLES</i>	Wall Modeled LES
<i>ZLES</i>	Zonal LES

### ***Small Letters***

$y^+$	Non-Dimensional distance of centroid of cell from the wall
$k$	Turbulent Kinetic Energy
$\mu_t$	Turbulent/Eddy Viscosity
$\Delta x$	Cell length in $x$ -direction on wall surface
$\Delta z$	Cell length in $z$ -direction on wall surface
$c, v$	Velocity of flow across a computational cell
$\Delta t$	Time step
$\mu_{sgs}$	Subgrid-scale viscosity
$\mu_{laminar}$	Laminar Viscosity
$r$	Radial direction of flow

### ***Capital Letters***

$C_\mu$	Constant
$D$	Diameter (Ref. geometrical dimension)
$D_0$	Diameter of nozzle exit
$P_s$	Static Pressure
$P_{ref}$	Reference Pressure
$R_{ij}$	Reynolds stress tensor
$Re$	Reynolds Number
$U_a$	Axial Velocity
$U_r$	Radial Velocity
$U_t$	Tangential Velocity
$U_{ref}$	Reference Velocity
$X$	$X$ -co-ordinate
$\mathbf{X}$	Position Vector

$Y$	$Y$ -co-ordinate
$Z$	$Z$ -co-ordinate

### ***Greek Symbols***

$\Delta$	Cell Size, Small Change
$\epsilon$	Turbulent kinetic energy dissipation rate
$\rho$	Density of air
$\mu$	Viscosity
$\theta$	Circumferential direction of flow
$\omega$	Vorticity Vector
$\Gamma$	Gamma Function

## **1 Introduction**

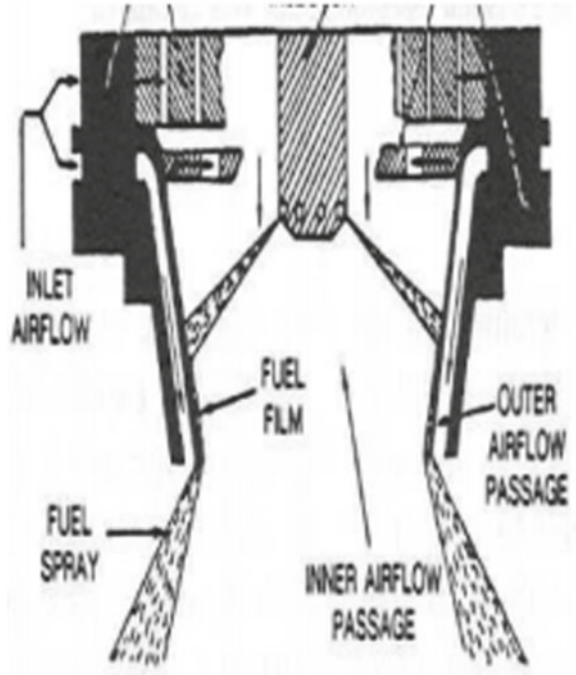
Improvement of specific fuel consumption through increase in thermal efficiency and that of specific thrust through burning of small air mass; both led to increment of pressure and temperature of gas turbine engines. According to Tacina [1], increases in pressure and temperature levels affect combustor in a way to the requirement of injector with large turn-down ratios meeting with parasitic requirements of uniform circumferential and radial temperature distributions and this is because of less amount of availability of dilution air for tailoring combustor exit temperature. With the injector in place and using different philosophies of combustor designs such as LPP, RQL, LDI, etc., NO<sub>x</sub> emissions of the combustor can be controlled where uniform mixture of fuel vapor and air burnt at low temperature. Hence, the injector plays a pivotal role to meet better combustion performances requirements with respect to combustion efficiency, flame stability, better ignition characteristics, lower emissions, etc. In terms of achieving lower droplet sizes and better near flow field of injector, the requirements are achieved through better atomization of bulk fuel into droplets and distribution of same in terms of lower sizes and velocities. According to Cornea [2], tool with deeper understanding and predictive capabilities from first principle is required in this respect and especially to understand unsteady phenomena involving complex three-dimensional geometries of interest and complex phenomena; it may require approaches such as discrete vortex method or Large Eddy Simulation. Zhang et al. [3] performed numerical CFD calculations using URANS model for flow over flat plate under with and without adverse pressure gradient effects. They captured large-scale vortical structures of the flow when reattachment occurs after a separated region due to adverse pressure gradient and vortical structure remains in the field despite large effective eddy viscosity produced by the turbulence model and the model does not capture the small-scale vortical

structures requiring smallest grid cells as required in LES. Sankaran and Menon [4] performed LES studies to capture unsteady interaction between spray dispersion, vaporization, fuel–air mixing, and heat release in a realistic combustor. They found that presence of high swirl increases the droplet dispersion, activates CTRZ, and reveals large-scale organized structures which are then subjected to complex stretch effects due to a combination of stream-wise and azimuthal vortical motions leading to enhanced fuel–air mixing. They opined that compared to RANS calculations where full range of length scales are not modeled, LES could resolve the flow/geometry-dependent large-scale motions more accurately and their study was confined to a geometry of dumb combustor with conical nozzle entry; boundary conditions of the LES simulations were, however, based on non-dimensional stream-wise and tangential velocity profiles available at the swirler exit plane, MPI-based parallel computation systems for interacting among processors, are used to perform the simulations. Stone [5], in his Ph.D. studies, performed LES calculations in a simplified high Re gas turbine combustor flows to capture vortex flame interaction, vortex dynamics, vortex breakdown, and combustion dynamics. Wang et al. [6] carried out LES study of gas turbine injector consisting of radial swirlers oriented in both co- and counter- rotating directions, to predict the characteristics of flow field. Results of the numerical analysis were compared with experimental data. Boundary conditions for inlet domain were applied after swirler exit upon superimposing broadband noise with a Gaussian distribution on the mean velocity profile with its intensity extracted from RANS simulation, and the methodology is iterated to its sensitivity. Block-based structured hexahedral grid system with mean cell size inside the injector as 0.35 mm was used during grid preparation, and four steps Runge–Kutta scheme for time integration and second-order accurate center-differencing methodology for spatial discretization were used for numerical calculation. The ratio of resolve to total TKE exceeded 95% in the bulk flow field. The axial, radial and tangential velocities downstream of the injector vis-à-vis the experimental results were plotted and reduced order POD analysis were also carried out to dictate most energetic components in the flow field. Wang et al. opined from their studies that air flow field inside injector is mainly dictated by primary swirler and the impact of secondary swirler on the same is limited.

Current LES study on the flow field was performed to understand flow field evolution. Since, the flow evolution especially inside the injector using single swirler is fundamental and to avoid difficulties for experimentally evaluating the same, authors were motivated to carry out this LES study. And most literatures showed that swirler exit conditions were derived from separate analysis and were used as boundary conditions for the LES domain.

In this present study, embedded LES method, new computational method, is adopted where no separate analysis was performed to impose boundary conditions on inlets to LES domain, rather than analyses were performed on the full computational domain segmented into multiple zones and total grids were generated based on varied zonal requirements with reduced computational costs. The flow field performances were predicted and comparisons were made between radial variations of

**Fig. 1** High shear swirl cup  
[8]



normalized axial velocities of LES predicted results and experimental PIV data at different downstream locations of the injector.

## 2 Computational Methodology

### 2.1 Model Details

As fundamental components of high-shear injector schematically shown in Fig. 1, the injector model under study is consisting of radial swirler attached with a conical nozzle at the exit of swirler as shown in Fig. 2. The geometrical swirl number and swirler vane angle are  $0.75^\circ$  and  $66.5^\circ$ , respectively. For details, refer [7]. Fluid volume of the injector is shown in Fig. 3.

### 2.2 Grid Details

The computational domain extends from 500 mm in upstream direction in a cylindrical duct of diameter 100 mm as per the experimental setup, and the exit flow of

**Fig. 2** Cut section of the mechanical model of the injector

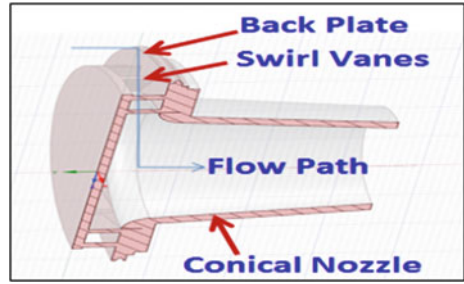
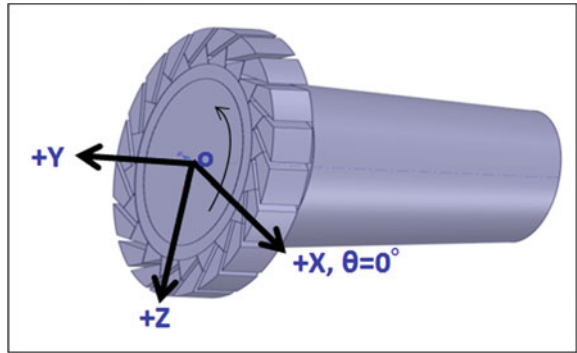


**Fig. 3** Fluid volume disposition of the injector at decomposed condition



the nozzle is allowed to meet on to a domain of length more than 1600 mm in a rectangular duct with square cross-section of size 780 × 780 mm as shown in Fig. 4. Size of upstream domain is based on experimental duct size. The square shape of size 780 × 780 mm is based on the understanding of better accommodating tangential swirl flows exiting from the conical nozzle without downstream wall confinement effects on flow evolution as well as having better grid. For further details, refer [7].

The total domain is divided into three zones: First zone covers flows from upstream inlet through swirler vanes flows exiting into nozzle connected downstream analyzed

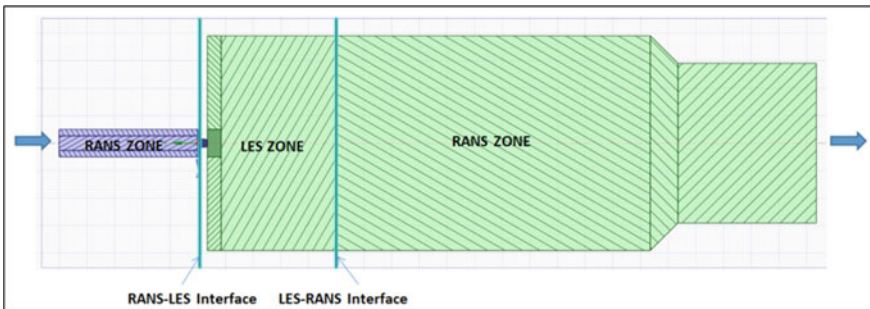


**Fig. 4** Computational domain used for the analysis

by RANS model (realizable  $k-\epsilon$  turbulence model with standard wall function); second zone covers RANS exit of first zone toward downstream of nozzle exit analyzed by LES model (wall-modeled LES); third zone includes toward the downstream of LES exit of second zone analyzed by same RANS model. Domains are seamlessly connected by capturing the interface fluid dynamics of the flow (discussed later).

Figure 5 shows grid details of the computational domain. The grid philosophies for the upstream and downstream RANS zones are kept same as in [7]. The densities of grids present in RANS zones are lesser because of non-resolving the scales there as shown in Fig. 5(a). Number of cells and size of grids required in the LES zone are based on the level of TKE to be resolved across the zone and accordingly the cell size  $\Delta x$  is arrived at. To make the turbulent model worked well, certain grid criteria is required to be met. As shown in Fig. 5(b), two layers of  $y^+$  adaptations were carried out to resolve the extend of wall  $y^+$  (150–200 were possible) keeping in view quality of grids such as skewness and minimum orthogonality requirement. The resulting aspect ratio of nozzle wall surface face sizes ( $\Delta x / \Delta z$ ), i.e., along wall parallel plane, is found to reach  $\sim 13$  which is more than the required value of maximum 2. However, aspect ratio based on cell-base length scale to cell wall distance is found to be 5.06 meeting the required acceptable limit of less than 10 [9]. Since, the phenomenon of interest is chosen to be away from wall, grid scheme of this order is considered to be acceptable. Time scale is worked out as  $\frac{\Delta}{v}$ , for which time step  $\Delta t$  is decided after ensuring that extend of smaller time step should lie in zone of interest. Cell size  $\Delta x$

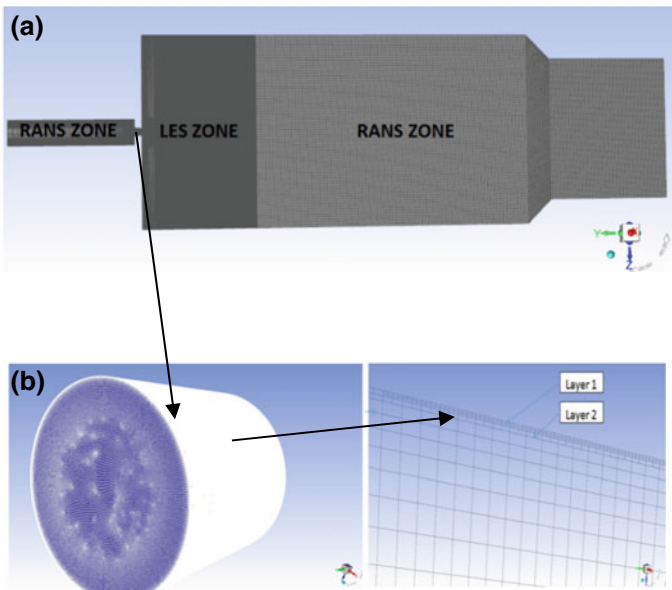


**Fig. 5** a Computational grid used for the simulation. b Details of the grid LES zone (nozzle portion)

and time step  $\Delta t$  are connected to CFL number as  $\frac{c\Delta t}{\Delta x}$ . CFL number is to be as close to 1 to resolve the time scale. Typical value of  $\Delta x$  is 0.1 mm and  $\Delta t$  is kept at  $1 \times 10^{-06}$  s during the computation.

A grid of size of 9.7 million having maximum skewness of 0.91 generated using ANSYS Meshing has been arrived at after resolving both time and length scales.

### 2.3 Solver Details

ANSYS Fluent version 19.2 was used for the analysis. Analyses were carried out considering the flow as unsteady, incompressible, iso-thermal, and turbulent. Realizable  $k-\varepsilon$  turbulence model is used in RANS zones. WMLES model was used in LES zone.

Time dependent RANS computations are performed as follows: The computations are performed after time averaging N-S equation resulting following set of equations which are required to be solved in CFD using finite volume methodology.

$$\rho \left( \frac{\partial \bar{u}_i}{\partial t} + \bar{u}_k \frac{\partial \bar{u}_i}{\partial x_k} \right) = -\frac{\partial \bar{p}}{\partial x_i} + \frac{\partial}{\partial x_j} \left( \mu \frac{\partial \bar{u}_i}{\partial x_j} \right) + \frac{\partial R_{ij}}{\partial x_j} \quad (1)$$

$$R_{ij} = -\rho \overline{u'_i u'_j} \quad (2)$$

$$R_{ij} = \mu_\tau \left( \frac{\partial \bar{u}_i}{\partial x_j} + \frac{\partial \bar{u}_j}{\partial x_i} \right) - \frac{2}{3} \mu_\tau \frac{\partial \bar{u}_i}{\partial x_j} \delta_{ij} - \frac{2}{3} \frac{\partial \bar{u}_i}{\partial x_j} \rho k \delta_{ij} \quad (3)$$

$$\mu_\tau = \rho C_\mu \frac{k^2}{\varepsilon} \quad (4)$$

$k$  and  $\varepsilon$  values are solved separately by using two different independent equations thus called the model as two equations model.

The general equations for LES computations are shown below.

In LES computations, large-scale turbulent structures are directly solved using resolved scales and small-scale effects are modeled and solved through filtering the N-S equation as like RANS calculations, but with more details. The filtered equations are formed by space averaging or Favre (density weighed averaging) averaging (based on incompressible or compressible flows) of N-S equation. Followings are the conservation equations applicable for incompressible computations:

According to [10], the space averaged filtered continuity and momentum equations are as follows:

$$\frac{\partial \rho}{\partial t} + \frac{\partial}{\partial x_i} (\rho \bar{u}_i) = 0 \quad (5)$$



$$\frac{\partial}{\partial t}(\rho \overline{u_i}) + \frac{\partial}{\partial x_j}(\rho \overline{u_i u_j}) = \frac{\partial}{\partial x_j}(\sigma_{ij}) - \frac{\partial \overline{p}}{\partial x_i} - \frac{\partial \tau_{ij}}{\partial x_j} \quad (6)$$

The molecular viscosity  $\sigma_{ij}$  is defined as

$$\sigma_{ij} \equiv \left[ \mu \left( \frac{\partial \overline{u_i}}{\partial x_j} + \frac{\partial \overline{u_j}}{\partial x_i} \right) \right] - \frac{2}{3} \mu \frac{\partial \overline{u_l}}{\partial x_l} \delta_{ij} \quad (7)$$

The subgrid-scale turbulent stress  $\tau_{ij}$  is defined as

$$\tau_{ij} \equiv \rho \overline{u_i u_j} - \rho \overline{u_i} \overline{u_j} \quad (8)$$

The subgrid-scale turbulent stress  $\tau_{ij}$  is computed from

$$\tau_{ij} - \frac{1}{3} \tau_{kk} \delta_{ij} = -2 \mu_t \overline{S_{ij}} \quad (9)$$

The isotropic part of the subgrid-scale stresses  $\tau_{kk}$  is not modeled but combined with the filtered static pressure term. The rate-of-strain tensor  $\overline{S_{ij}}$  for the resolved scale is defined by

$$\overline{S_{ij}} \equiv \frac{1}{2} \left( \frac{\partial \overline{u_i}}{\partial x_j} + \frac{\partial \overline{u_j}}{\partial x_i} \right) \quad (10)$$

where  $\mu_t$  is modeled based on type of LES model requirement.

In current numerical simulation based on ELES or ZLES model, LES portion of the simulation is resolved using algebraic WMLES model, and  $\mu_t$  has been defined accordingly. In WMLES, inner part of logarithmic turbulent layer is solved through zero-equation algebraic RANS, and outer part of turbulent boundary layer is solved through a modified LES formulation reducing LES grid requirement for high Re flows. The procedure could be useful when phenomena were considered away from wall, and wall boundary layers need not to be resolved.

In WMLES, eddy viscosity  $\nu_t$  is calculated below with the use of a modified grid scale  $\Delta$  to take care of grid anisotropies in wall-bounded flows:

$$\nu_t = \min \left[ (\kappa d_w)^2, (C_{\text{Smag}} \Delta)^2 \right] \cdot S \cdot \left\{ 1 - \exp \left[ - \left( y^+ / 25 \right)^3 \right] \right\} \quad (11)$$

where  $d_w$ : wall distance,  $S$ : strain rate,  $\kappa = 0.41$  and  $C_{\text{Smag}} = 0.2$  are constants,  $y^+$ : normal to wall inner scaling, and modified grid scale  $\Delta$  is given as:

$$\Delta = \min(\max(C_w \cdot d_w; C_w \cdot h_{\max}, h_{\text{wn}}); h_{\max}) \quad (12)$$

where  $h_{\max}$ : maximum edge length for a rectilinear hexahedral cell which is modified for other cell types and/or conditions based on an extension of this concept.  $h_{\text{wn}}$ : wall-normal grid spacing, and  $C_w = 0.15$  is a constant.

Mass flow inlet and pressure outlet boundary conditions with air as computational fluid have been chosen for the analysis. All walls are considered to be at adiabatic conditions. At interior zone of the RANS–LES interface, vortex method is used to resolve turbulence from the modeled turbulence of upstream RANS calculations. According to [10], numbers of vortices are assessed through  $N/4$ , where  $N$  is number of cell faces and the vorticity transport is modeled and tracked as follows:

$$\omega(X, t) = \sum_{k=1}^N \Gamma_k(t) \eta(|X - X_k|, t) \quad (13)$$

Corresponding fluctuating velocity field computed using the Biot–Savart law as:

$$u(X, t) = -\frac{1}{2\pi} \iint \frac{(X - X') \times \omega(X') e_z}{|X - X'|^2} dX' \quad (14)$$

However, for the LES–RANS interface, “no perturbations” conditions were imposed so as to have a smooth transitions of flow from LES to RANS. Here, downstream RANS domain uses mean flow of LES, since perturbations are considered to be diminished at the interface.

For numerical computations, second-order upwind scheme for spatial resolutions for momentum, turbulent KE, etc., and second-order implicit scheme for time resolutions were used. SIMPLEC scheme was used for pressure velocity coupling. Residuals for convergence criteria were kept at  $10^{-06}$ .

### 3 Results and Discussion

Results of CFD analysis are discussed in this section. It consists of time-dependent contour, vector, streamlines, and turbulent kinetic energy plots of the flow field. Data were captured after running simulations for much over five flow-through times through the computational domain (typical value for five flow-through times is  $\sim 0.013$  s and data were recorded and time averaging was performed after  $\sim 0.03$  s ensuring better stability in flow). SGS viscosity ratio  $\left(\frac{\mu_{\text{sgs}}}{\mu_{\text{laminar}}}\right) \sim 500$ , which is found to be lower than turbulent viscosity ratio calculated from RANS simulation as expected, thus ensuring dissipating nature of turbulence due to LES calculations (turbulent viscosity ratio from RANS calculation was 2200). Apart from this, it was also found from analysis that resolved spectrum in flow of interest (ratio of resolved TKE to the sum of resolved TKE and resolved TKE due to SGS averaging) is 97%, which

directly builds confidence of carrying out analysis using current model setup, length, and time scales resolved, etc.

### 3.1 Comparison of Normalized Velocities

Figure 6 shows comparison of normalized time averaged axial velocities between numerical prediction and experimental PIV results at different downstream locations of exit of the injector showing first-order dynamics of the system.

Results show there is a good agreement with the experimental data; the variations between them are lower.

Normalized time averaged radial and tangential velocities based on the numerical prediction are shown in Figs. 7 and 8, respectively.

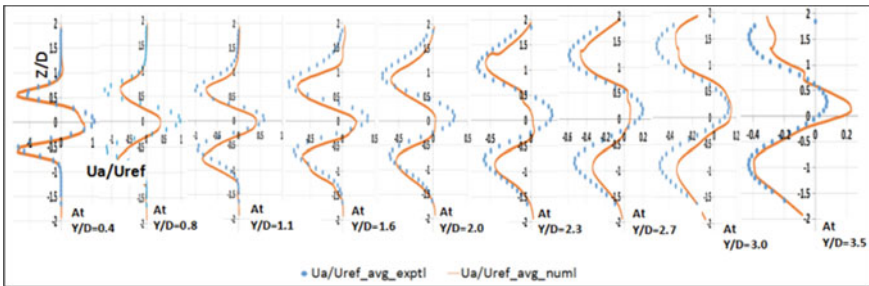


Fig. 6 Time averaged normalized axial velocity comparison

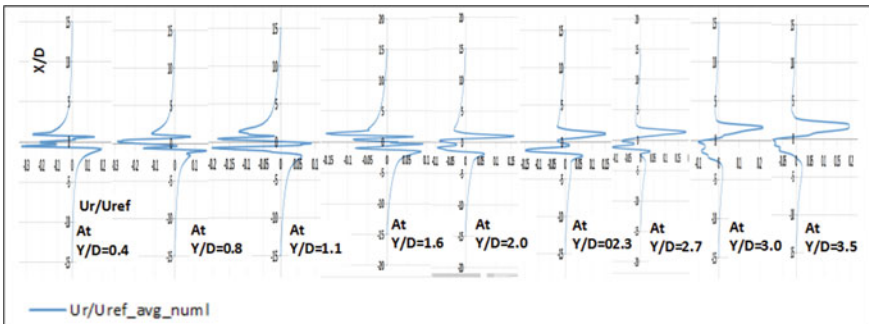
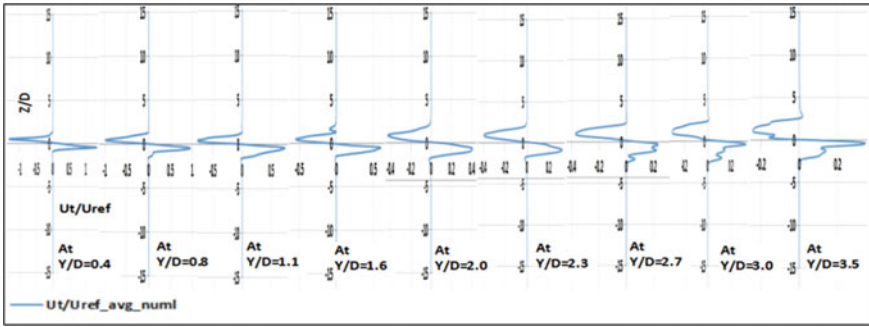


Fig. 7 Numerical prediction of time averaged normalized radial velocity variations along the injector axis



**Fig. 8** Numerical prediction of time averaged normalized tangential velocity variations along the injector axis

### 3.2 Various Plots

#### 3.2.1 Q-criteria

Figure 9 clearly shows presence of vortex inside and downstream of injector as it flows.

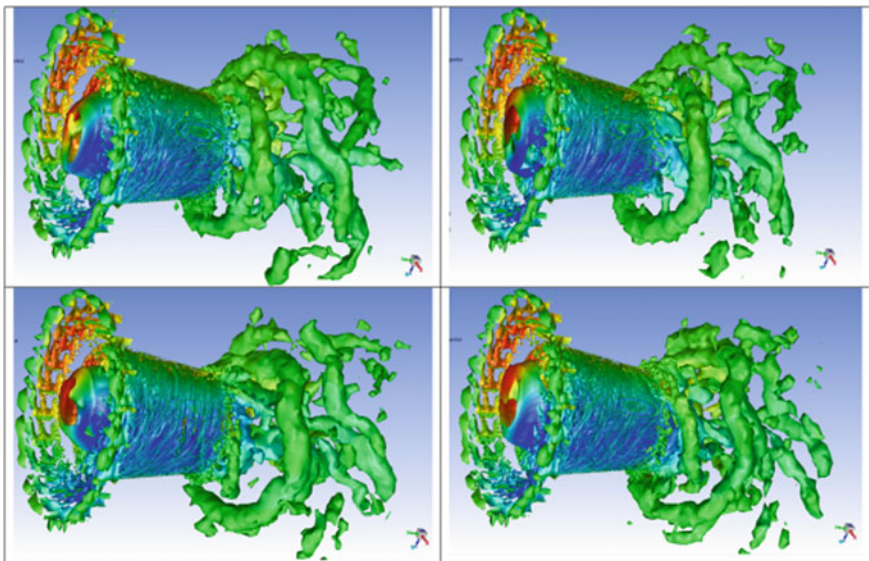


**Fig. 9** Q-criteria iso-surface (based on 1% of maximum value at  $Z = 0$  plane at location of interest) colored by tangential velocity: Data are plotted for every 0.1 ms time interval after mean flow fields were stabilized

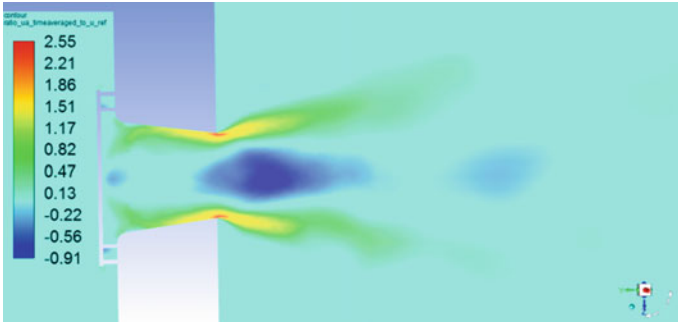


Fig. 10 Normalized time averaged axial velocity contour

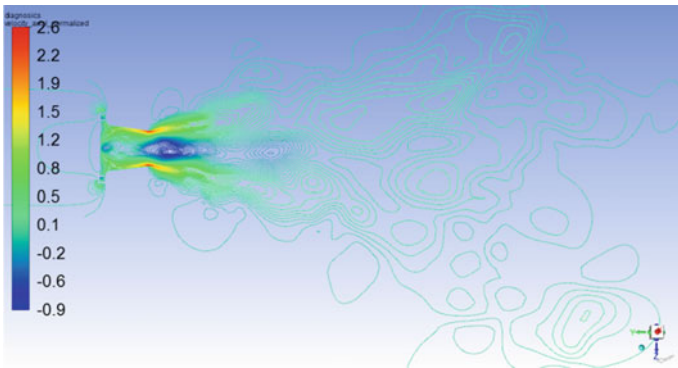


Fig. 11 Normalized time averaged axial velocity streamlines

### 3.2.2 Contour Plots of Axial Velocity

Figure 10 shows above contour plot of the normalized axial velocity showing recirculation zone near to exit of the injector.

### 3.2.3 Stream Line Plots

Figure 11 shows streamline plot of normalized axial velocity showing recirculation zone near to exit of the injector.

### 3.2.4 Vector Plots of Axial Velocity ( $r$ - $y$ ) and ( $r$ - $\theta$ ) Directions

Figure 12 shows time averaged velocity vector plot colored by normalized axial velocity showing recirculation zone near to exit of the injector. There is also presence

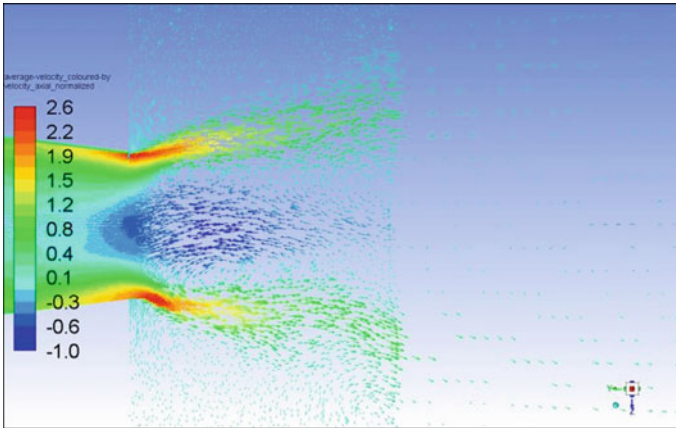


Fig. 12 Time averaged velocity vector colored by normalized axial velocity

of shear layer which fluctuates and vortices were also present due to K–H instability. This instability to atomize fuel film can be added up to that created by secondary swirler at the same location (Fig. 13).

Through above vector plots multiple phenomena are being tracked: In above plot (Fig. 13), normalized vorticity of flow is super-imposed on normalized axial velocity. It is seen high vortex started from swirler exit gradually reduces with flow with maximum vorticity occurring near injector wall when flow is inside the injector. Presence of vortex near the wall is due to presence of PVC (not shown here) at

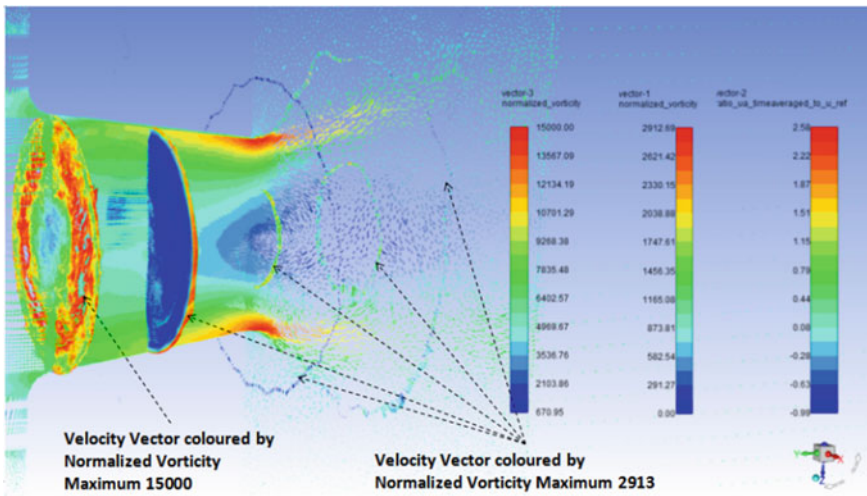
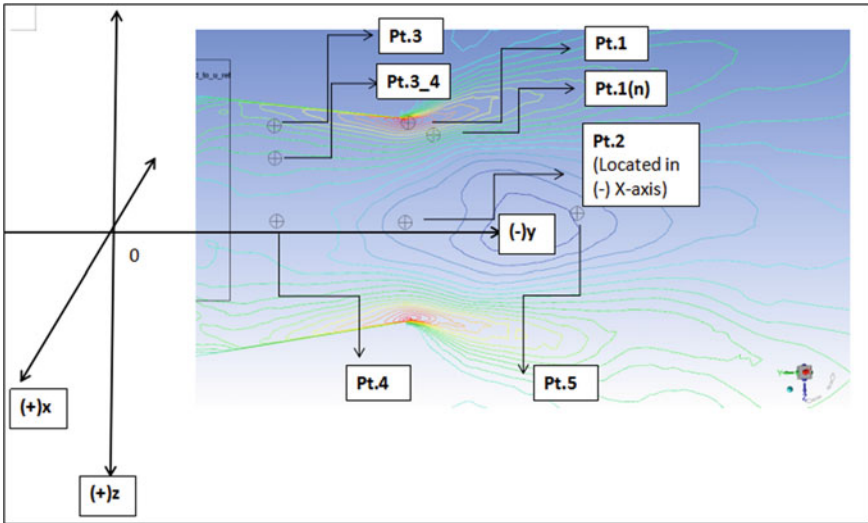


Fig. 13 Normalized vorticity-velocity fields



**Fig. 14** Positions of various monitoring points for time-dependent tracking of various parameters

injector core, which continuously throws out air toward the wall. According to Shanmugadhas and Chakravarthy [9], PVC with primary spray continuously precessed due to primary air swirl which indirectly creates periodic droplet impingement on the wall and thereby forming non-uniform filming of fuel on the pre-filming wall. It is also seen that around the periphery of CTRZ magnitude of normalized vorticity is slightly higher than that near to the shear layer: This may also help to atomize and disperse the fuel droplets (Fig. 13).

### 3.2.5 Plots and Capturing Frequency Tracks

During the simulation run, time-based values of parameters such as  $U_a$ ,  $U_t$ ,  $U_r$ , and  $P_s$  are collected and stored at each of the locations mentioned above (refer Fig. 14) at each time step  $1 \times 10^{-06}$  s. These parameters are then plotted (refer Fig. 15) to reveal for any periodic phenomena.

Figure 15 shows the plotting of periodic signals captured w.r.t. time after removing initial transient data. FFT of the signals is shown in Fig. 16. Here, it may be mentioned that during the simulation run, it was observed that after flow-time of  $\sim 0.0524$  s the time averaged values of parameters have been found to be varied within maximum  $\pm 2\%$  of their mean values (results not shown here). And since this variation is small, hence, the solution was considered to be achieved statistically averaged value.

From Fig. 16, it is seen that at core of the injector near to axis and slightly away from injector tip, there are phenomena with 2.5 kHz frequency. This frequency can be considered for PVC and shear layer fluctuations.

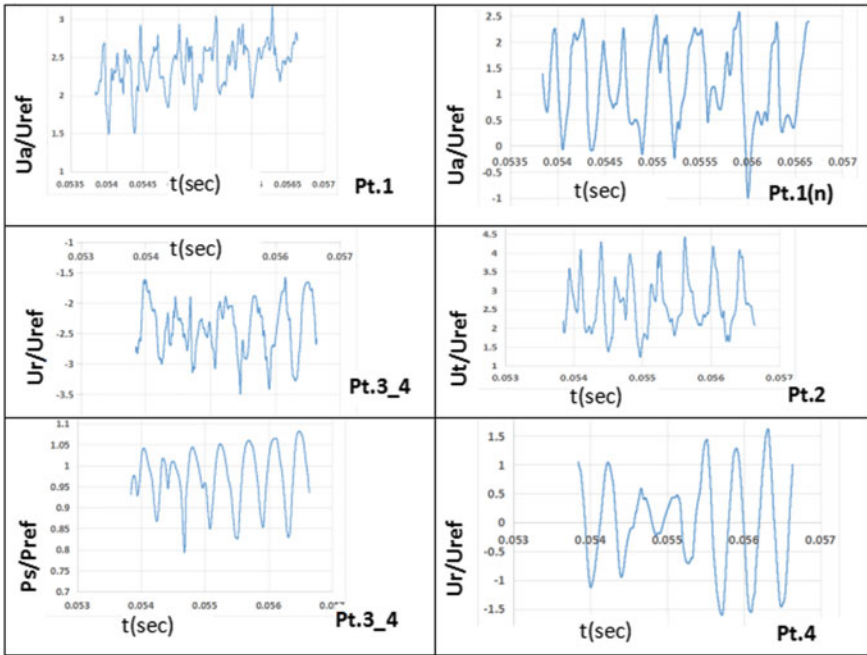


Fig. 15 Time-dependent signals of parameters at various monitoring points of the flow field collected over 2.8 ms

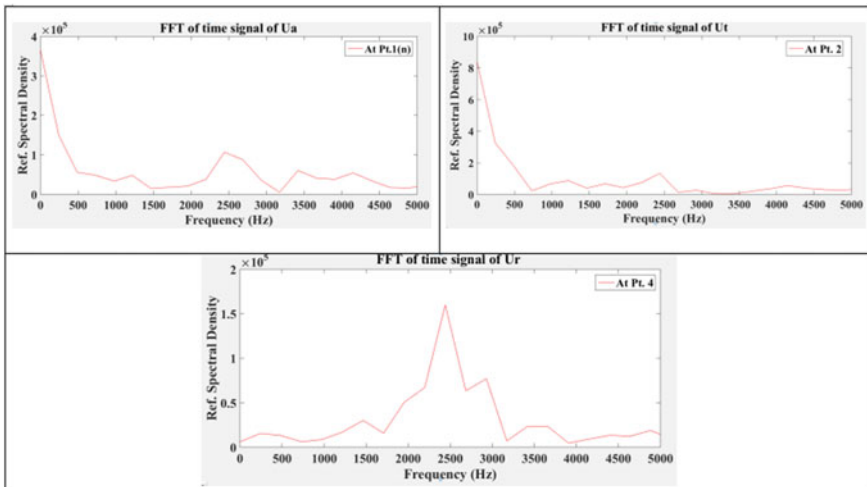
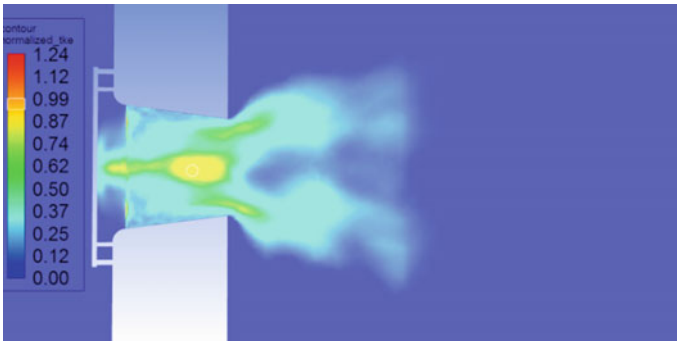


Fig. 16 FFT of respective time-dependent signals (second column of Fig. 15) showing various frequencies





**Fig. 17** Normalized TKE plot of the flow field

### 3.2.6 Turbulent KE Plots

Figure 17 clearly shows that most values of normalized TKE exist near the core and tip of the injector. Presence of TKE at starting of core is due to PVC, slightly at downstream TKE is due to presence of CTRZ; both these TKE would be useful for proper mixing of fuel–air droplets; where TKE presence near to injector lip would be helpful for fuel atomization and droplet dispersion. The spatial energetic modes could also be extracted using reduced order mathematical tool such as POD.

## 4 Conclusions

LES analysis is able to capture reasonably the flow field of a fuel injector fitted with single radial swirler, thus capturing important fundamental aspects of flow physics. WMLES model of ANSYS Fluent was used to capture turbulence in LES region. Closure trend behavior of numerical results and experimental data of the axial velocity shows that aspects of modeling for resolving the flow field are reasonable. Analysis could capture different vortices present in flow field useful for fuel atomization and droplet dispersion for proper mixing. It was found that vorticity present near to the injector wall surface and outer periphery of CTRZ (with which PVC fluctuates) could be useful for creating azimuthal instabilities on the fuel film and relevant frequency is 2.5 kHz. Positions of higher TKE fields have shown relevant phenomena in terms of fuel atomization and droplet dispersion. Modeling methodologies used here would be very useful for carrying out computational studies and database generation for the kind of complex geometry and physics. Since this preliminary study is aimed at considering a fixed location of the interfaces, studies can be further progressed by varying the placement of interface zones and their impacts on flow field so as to make the model more robust.

**Acknowledgements** Authors are very much grateful to Mr. M. Z. Siddique, DS & Director, Gas Turbine Research Establishment, Bangalore, for permitting to present this paper in the conference. The authors are also thankful to members of combustion group for their support and help extended during the course of the study.

## References

1. Tacina R (1990) Combustor technology for future aircraft. NASA Technical Memorandum 103268 AIAA-90-2400
2. Correa SM (1998) Power generation and aero propulsion gas turbines: from combustion science to combustion technology. In: Twenty-seventh symposium (international) on combustion. The Combustion Institute, pp 1793–1807
3. Zhang HL, Bachman CR, Fasel HF (2000) Reynolds-averaged Navier-Stokes calculations of unsteady turbulent flow. AIAA-0143
4. Sankaran V, Menon S (2002) LES of spray combustion in swirling flow. *J Turbul* 3:N11. <https://doi.org/10.1088/1468-5248/3/1/011>
5. Stone C (2003) Large eddy simulation of combustion dynamics in swirling flows. PhD Thesis. Georgia Institute of Technology, School of Aerospace Engineering March 2003
6. Wang S, Yang V, Hsiao G, Hsieh SY, Mongia HC (2007) Large-eddy simulations of gas-turbine swirl injector flow dynamics. *J Fluid Mech* 583:9–122 (Cambridge University Press)
7. Rana R, Sonukumar, Muthuveerappan N (2019) RANS based iso-thermal CFD analysis of the flow field created by a radial swirler in a conical nozzle. GTINDIA2019-2726, <https://doi.org/10.1115/GTINDIA2019-2726GTIndia>
8. Cohen JM, Rosfjord TJ (1993) Influences on the sprays formed by high shear fuel nozzle/swirler assemblies. *J Propul Power* 9(1) Jan-Feb 1993
9. Shanmugasdas KP, Chakravarthy SR (2018) Wall filming and atomization inside a simplified prefilming coaxial swirl injector: role of unsteady aerodynamics. In: 2018 AIAA aerospace sciences meeting, 8–12 Jan 2018, Kissimmee, Florida
10. ANSYS (2016) ANSYS fluent theory guide